

# Gravity currents in horizontal porous layers: transition from early to late self-similarity

M. A. HESSE<sup>1</sup>, H. A. TCHELEPI<sup>1</sup>†,  
B. J. CANTWELL<sup>2</sup> AND F. M. ORR JR<sup>1</sup>

<sup>1</sup>Department of Energy Resources Engineering, Stanford University, Stanford CA 94305, USA

<sup>2</sup>Department of Aeronautics and Astronautics, Stanford University, Stanford CA 94305, USA

(Received 30 March 2006 and in revised form 26 October 2006)

We investigate the evolution of a finite release of fluid into an infinite, two-dimensional, horizontal, porous slab saturated with a fluid of different density and viscosity. The vertical boundaries of the slab are impermeable and the released fluid spreads as a gravity current along a horizontal boundary. At early times the released fluid fills the entire height of the layer, and the governing equation admits a self-similar solution that is a function of the viscosity ratio between the two fluids. This early similarity solution describes a tilting interface with tips propagating as  $x \propto t^{1/2}$ . At late times the released fluid has spread along the boundary and the height of the current is much smaller than the thickness of the layer. The governing equation simplifies and admits a different similarity solution that is independent of the viscosity ratio. This late similarity solution describes a point release of fluid in a semi-infinite porous half-space, where the tip of the interface propagates as  $x \propto t^{1/3}$ . The same simplification of the governing equation occurs if the viscosity of the released fluid is much higher than the viscosity of the ambient fluid. We have obtained an expression for the time when the solution transitions from the early to the late self-similar regime. The transition time increases monotonically with increasing viscosity ratio. The transition period during which the solution is not self-similar also increases monotonically with increasing viscosity ratio, for mobility ratios larger than unity. Numerical computations describing the full evolution of the governing equation show good agreement with the theoretical results. Estimates of the spreading of injected fluids over long times are important for geological storage of CO<sub>2</sub>, and for the migration of pollutants in aquifers. In all cases it is important to be able to anticipate when the spreading regime transitions from  $x \propto t^{1/2}$  to  $x \propto t^{1/3}$ .

---

## 1. Introduction

Density-driven flows in porous media are common in geological problems and in engineering applications. In the absence of fluid sinks and sources, such as wells, buoyancy is the main driving force for subsurface transport. The density differences may arise due to concentration or temperature gradients within the same fluid or due to density differences between two immiscible fluid phases. The currents arising from these density differences are often called gravity currents or gravity tongues. Hydrological examples include the evolution of the groundwater table, and the migration of

† Author to whom correspondence should be addressed.

pollutants in aquifers (Bear 1972). Water and gas flooding of hydrocarbon reservoirs are examples of applications in petroleum engineering (Lake 1989).

### 1.1. Carbon dioxide storage in saline aquifers

This study is motivated by carbon capture and storage, also known as CO<sub>2</sub>-sequestration, in deep geological formations. It has been suggested as a way to reduce greenhouse gas emissions and to mitigate global climate change (Metz *et al.* 2006). In the temperature and pressure range encountered in geological CO<sub>2</sub> storage, the density of the CO<sub>2</sub>-vapour is less than the density of the brine (Bachu 2003). CO<sub>2</sub> can be stored in aquifers that are overlain by an impermeable seal that forms a barrier to upward migration of CO<sub>2</sub>-vapour. The buoyant CO<sub>2</sub>-vapour will spread underneath the seal and along the top of the aquifer as a gravity current. An estimate of the area invaded by CO<sub>2</sub>-vapour is of great interest during site selection and subsequent monitoring efforts.

When CO<sub>2</sub> is stored in saline aquifers the injection period may be several decades, but the CO<sub>2</sub>-plume continues to migrate for several hundreds or thousands of years. To study the long-term evolution of the injected fluid we can neglect the details of the short injection period. The distribution of the fluids at the end of the injection period simply provides an initial condition for the long-term evolution. Given this simplification, we are interested in the evolution of a finite release of fluid into a saturated porous medium, with a particular initial distribution. Owing to the diffusive nature of the governing equations (see §2.1) the details of the particular shape of the initial condition have a small effect on the intermediate and long-term evolution (see §3.3).

### 1.2. Previous work on hydrostatic sharp interface flows

Similar mathematical models have been developed independently in different disciplines. We will refer to them as hydrostatic sharp interface flows. They are based on two main dynamic assumptions: (1) the fluids are completely segregated and therefore separated by a sharp interface, (2) the pressure distribution in both fluids is hydrostatic, and the flow is approximately parallel to the boundary of the domain. The second assumption is analogous to the lubrication approximation in clear fluids (Huppert 1982). In hydrology this assumption is called Dupuit's approximation, and it gives rise to Boussinesq's equation (Bear 1972), also known as the porous medium equation. In petroleum engineering this set of assumptions is called the concept of vertical equilibrium (Yortsos 1995), and gives rise to Dietz's equation (Dietz 1953).

It is also common to assume an infinitely deep porous half-space. In reality aquifers and reservoirs often have very high aspect ratios (length : height > 100 : 1), and do not resemble a half-space. The half-space assumption has been very successful in modelling the groundwater table, because the viscosity of the surrounding air is negligible. If the viscosity of the surrounding fluid is not negligible this approximation must be justified more carefully. In this case the half-space solution is only recovered in the limit of a very thin gravity current. How thin the gravity current needs to be for this approximation to become valid depends on the viscosity of the ambient fluid. In the general case the flow must be considered in the context of a layer of finite thickness, and the full equations have to be solved.

Similarity solutions can be obtained for both the full equations and the simplified porous medium equation. Recently both types of solutions have been applied to CO<sub>2</sub> storage in saline aquifers. Lyle *et al.* (2005) model the injection of CO<sub>2</sub> into a half-space, while Nordbotten, Celia & Bachu (2005) consider injection into a layer of finite thickness. Lyle *et al.* (2005) note that their scaling laws differ from those obtained

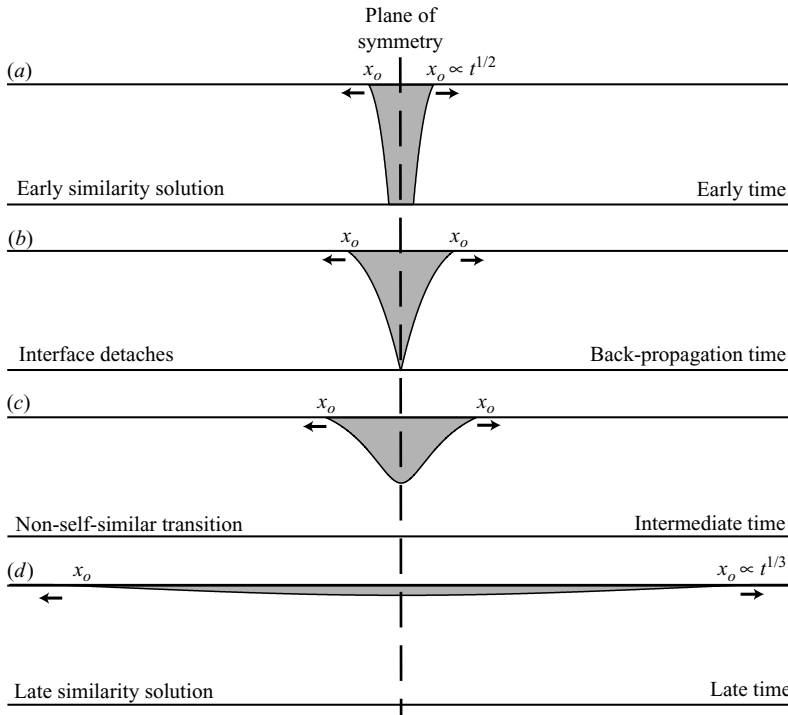


FIGURE 1. The evolution of buoyant  $\text{CO}_2$ -vapour (grey) released into a horizontal porous layer saturated by brine (white). The outward propagating tip of the interface is marked by  $x_o$ . All figures are exaggerated in the vertical direction, to make the late solution (d) visible. In many situations of interest the width of the invaded region in (a) is several times larger than the aquifer height.

by Nordbotten *et al.* (2005). This difference is partly due to the different injection configuration: Nordbotten *et al.* (2005) assume injection over the whole depth of the aquifer, while Lyle *et al.* (2005) consider injection from a point source at the top of the aquifer. The difference in the geometry of the domain is probably the main reason for the difference in the scaling laws. We show that a change in the effective size of the domain is enough to change the scalings of a gravity current formed from a finite release of fluid.

## 2. Problem statement

For two-dimensional problems the similarity solution to the full equation predicts that the tip of the interface propagates as  $x \propto t^{1/2}$ , while the similarity solution to the porous medium equation predicts tip propagation as  $x \propto t^{1/3}$ . The thickness of a gravity current formed by a finite release of fluid decreases monotonically over time and the porous medium equation will become applicable at late times. Therefore the tips of the fluid interface will initially propagate as  $x \propto t^{1/2}$  and later as  $x \propto t^{1/3}$  (figure 1). When this transition occurs and how the transition time depends on the mobility ratio between the fluids are important questions that we address in this paper.

### 2.1. Governing equation

We consider the flow of fluid 1 with density  $\rho_1 = \rho$  and viscosity  $\mu_1$  and of fluid 2 with density  $\rho_2 = \rho + \Delta\rho$  and viscosity  $\mu_2$  in a horizontal porous layer of thickness  $H$  and

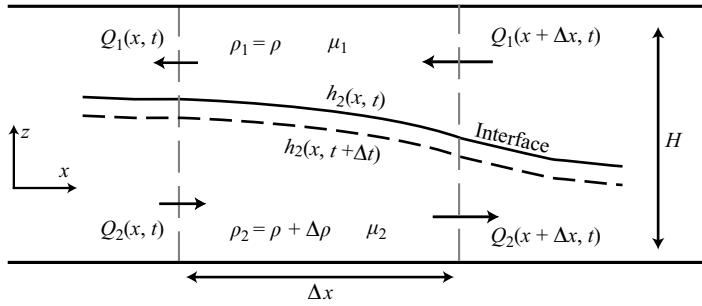


FIGURE 2. The geometry of the porous layer and the variables used in the derivation in §2.1.

infinite lateral extent (figure 2). We assume that the porous medium is homogeneous and isotropic with permeability  $k$  and porosity  $\phi$ , and that the top and the bottom boundaries are impermeable. The fluids are separated by a sharp interface, we denote the thickness of each fluid by  $h_p[x, t]$  where  $p \in \{1, 2\}$ , so that  $h_1[x, t] + h_2[x, t] = H$ . We consider an aquifer with a large aspect ratio (length : height  $\gg 1$ ), so that we can assume hydrostatic pressure in both fluids, and the vertical velocity is small. An asymptotic analysis of this simplification has been presented by Yortsos (1995). In this case the pressure distribution in the layer is given by

$$p = \begin{cases} p_I - g\rho(z - h_2) & \text{for } z > h_2, \\ p_I - g(\rho + \Delta\rho)(z - h_2) & \text{for } z \leq h_2, \end{cases} \quad (2.1)$$

where  $p_I$  is the unknown pressure at the interface and  $g$  is the gravitational acceleration. The volume flux per unit width  $q_p$  of phase  $p$  is given by Darcy’s law  $q_p = -k\lambda_p \partial p / \partial x$ , where we introduce the mobility of phase  $p$  defined as  $\lambda_p = k_{rp}^* / \mu_p$ . In this study we assume that the fluids are completely segregated, so that the end-point relative permeabilities are unity  $k_{rp}^* = 1$ , and the mobility becomes  $\lambda_p = 1 / \mu_p$ . The flow rate per unit width of phase  $p$  is given by  $Q_p = h_p q_p$ . Inserting the expression for the pressure into the flow rates, we obtain

$$Q_1 = -h_1 k \lambda_1 \left( \frac{\partial p_I}{\partial x} - g\rho \frac{\partial h_1}{\partial x} \right) \quad \text{and} \quad Q_2 = -h_2 k \lambda_2 \left( \frac{\partial p_I}{\partial x} + g(\rho + \Delta\rho) \frac{\partial h_2}{\partial x} \right).$$

In the absence of a source term the global conservation of volume is given by  $Q_2 + Q_1 = 0$ . Using this constraint we can eliminate  $\partial p_I / \partial x$  from the expressions for the flow rates and obtain

$$Q_2 = -Q_1 = -kg\Delta\rho \frac{h_2 \lambda_2 h_1 \lambda_1}{h_2 \lambda_2 + h_1 \lambda_1} \frac{\partial h_2}{\partial x}.$$

Both flow rates vanish if the mobility or height of either fluid is zero. It has been shown that this leads to a finite propagation speed of the fronts (Barenblatt & Vishik 1956). To obtain an equation for the evolution of the interface, we consider the conservation of the volume of released fluid  $p$  over region  $\Delta x$  and time  $\Delta t$  as shown in figure 2. The change in volume  $\Delta V_p$  is given by  $\Delta V_p = \Delta h_p \Delta x \phi = (Q_p|_x - Q_p|_{x+\Delta x}) \Delta t$ . Inserting the expression for  $Q_p$  into the volume balance and taking limits for small  $\Delta x$  and  $\Delta t$ , the equation for the evolution of the interface between the fluids is given by

$$\frac{\partial h_p}{\partial t} = \kappa_p \frac{\partial}{\partial x} \left( \frac{h_p(H - h_p)}{h_p(M_p - 1) + H} \frac{\partial h_p}{\partial x} \right), \quad (2.2)$$

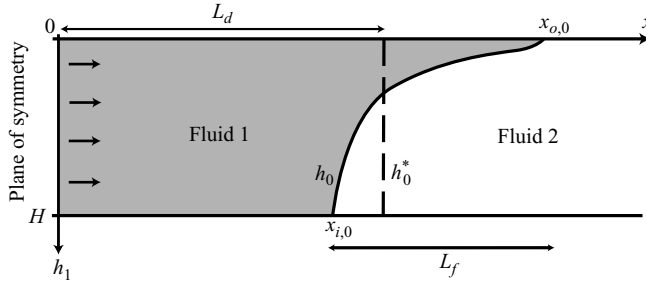


FIGURE 3. The geometry of the initial condition and the three associated length scales  $H$ ,  $L_d$ , and  $L_f$ . A particular initial condition  $h_0[x]$  and the corresponding idealized step function initial condition  $h_0^*[x]$  are shown. The arrows indicate that the fluid has been injected over the whole depth of the reservoir.

where we have introduced two parameters, the conductivity of the released fluid  $p$  given by  $\kappa_p = kg\Delta\rho\lambda_p/\phi$  and the mobility ratio  $M_p = \lambda_p/\lambda_q = \mu_q/\mu_p$ , where the subscript  $q$  denotes the ambient fluid. Note that the parameters are not independent;  $\lambda_p$  occurs in both. This choice of parameters allows a simple reduction of (2.2) in the limits  $\max(h_p[x, t]) \ll H$  or  $M_p \ll 1$ , as discussed in §4.1. In these limits the equation loses its dependence on  $M_p$ , but retains the parameter  $\kappa_p$ . To allow this reduction  $\kappa_p$  must be defined in terms of the mobility of the released fluid, and must be independent of the mobility of the ambient fluid. Equation (2.2) is invariant under the substitution

$$h_p = H - h_q, \quad M_p = M_q^{-1}, \quad \kappa_p = \kappa_q M_p = \frac{\kappa_q}{M_q}. \quad (2.3)$$

This transformation can be used to obtain a similar expression for the evolution of the thickness of the ambient fluid  $h_q$  from (2.2). Equation (2.2) is expressed in terms of the subscript  $p$  only, and we drop it to simplify the notation.

## 2.2. Initial and boundary conditions

We consider the evolution of the interface after injection has stopped ( $t \geq t_0$ ). Figure 3 illustrates the initial condition with  $\text{CO}_2$  injection into a saline aquifer. We assume that fluid has been injected along the whole depth of the layer, and has formed a gravity tongue along the upper boundary of the porous layer (Riaz & Tchelepi 2006). It is common to inject fluid over the whole depth of the aquifer to increase the injection rate, and to distribute the fluid evenly throughout the depth of the aquifer. The latter is desirable during  $\text{CO}_2$  storage, to increase dissolution of the  $\text{CO}_2$  into the ambient brine and to increase trapping of  $\text{CO}_2$  bubbles by capillary forces.

Near the injection site the gas has completely displaced the water over an average distance of  $L_d$ . The lateral extent of the fluid invasion is determined by the viscous to gravity ratio  $R_{vg} = (u/L_d)/(u_g/H) = (u\mu_g H)/(k\Delta\rho g L_d)$ , where  $u$  is the average horizontal flow velocity, and  $u_g = k\Delta\rho g/\mu$  is a gravitational velocity (for detailed discussion see Tchelepi 1994). When  $R_{vg}$  is small, gravitational forces dominate the flow, and a thin gravity tongue forms at the top of the aquifer. When  $R_{vg}$  is large, the interface advances over the whole depth of the aquifer.  $L_d$  increases with time during the injection period and  $R_{vg}$  generally decreases over time. During  $\text{CO}_2$  storage large quantities of fluid are injected and the horizontal velocity  $u$  is high and  $R_{vg}$  is initially large. Initially the interface advances over the whole depth of the aquifer. Over time  $R_{vg}$  decreases and a gravity tongue will form, leading to the initial condition shown in figure 3.

The gas–water interface transitions from  $h_0[x_{i,0}] = H$  to  $h_0[x_{o,0}] = 0$  over a frontal region of width  $L_f = x_{o,0} - x_{i,0}$ . The volume of gas is given by the integral over the initial distribution

$$V = 2\phi \int_0^{x_{o,0}} H - h_0 \, dx. \quad (2.4)$$

The length scale  $L_d$  is chosen so that an idealized step function initial profile located at  $x = L_d$  has the same gas volume as the particular initial condition ( $V = 2\phi L_d H$ ). The idealized initial condition is

$$h_0^* = \begin{cases} H & \text{for } |x| \leq L_d, \\ 0 & \text{for } |x| > L_d. \end{cases}$$

This initial configuration imposes three length scales: the layer height  $H$ , the average displacement distance  $L_d$ , and the width of the front at the end of injection  $L_f$  (figure 3). The two boundary conditions for (2.2) require that  $h[x, t] \rightarrow 0$  for  $|x| \rightarrow \infty$ .

### 3. Self-similar solution at early times

For  $L_f < L_d$  the fronts are initially separated, and the finite propagation speed of the interface tips ensures that the fronts will evolve independently until their inward propagating tips collide (figure 1*b*). As a result each front can be analysed in isolation, and it is convenient to shift it to the origin ( $\hat{x} = x - L_d$ ), so that the initial condition becomes

$$\hat{h}_0 = \begin{cases} H & \text{for } \hat{x} \leq \hat{x}_{i,0}, \\ h_0[\hat{x} + L_d] & \text{for } \hat{x}_{i,0} < \hat{x} < \hat{x}_{o,0}, \\ 0 & \text{for } \hat{x} \geq \hat{x}_{o,0}. \end{cases}$$

The new boundary conditions are

$$\hat{h}[\hat{x} \rightarrow -\infty] = H, \quad \hat{h}[\hat{x} \rightarrow \infty] = 0. \quad (3.1)$$

The early evolution of the interface is independent of the front separation  $2L_d$ , but the duration of this early period depends on  $L_d$ .

#### 3.1. Dimensional analysis

We follow the general procedure for dimensional analysis given by Barenblatt (1996). The problem defined above has three dimensions: length  $L$ , height  $H^*$ , and time  $T$ . The dimensions of the variables and parameters appearing in (2.2) and the initial condition are

$$[\hat{h}] = [H] = H^*, \quad [\hat{x}] = [L_f] = L, \quad [t] = T, \quad [\kappa] = L^2 H^{*-1} T^{-1}, \quad [M] = 1.$$

The parameters  $\kappa$ ,  $H$ , and  $t$  have independent dimensions and give the length scale  $l = (\kappa H t)^{1/2}$ . We obtain the dimensionless parameters

$$\Pi = \frac{\hat{h}}{H}, \quad \Pi_1 = \zeta = \frac{\hat{x}}{(\kappa H t)^{1/2}}, \quad \Pi_2 = \zeta_f = \frac{L_f}{(\kappa H t)^{1/2}}, \quad \Pi_3 = M. \quad (3.2)$$

The non-dimensional interface height  $\Pi$  can be written as a dimensionless function  $\psi$  of the dimensionless variables  $\Pi = \psi[\Pi_1, \Pi_2, \Pi_3]$ . We seek a similarity solution for times after the details of the particular initial condition have disappeared. As time increases  $\Pi_2 \rightarrow 0$ , while  $\Pi_3$  remains finite, and  $\hat{x}$  can always be chosen so

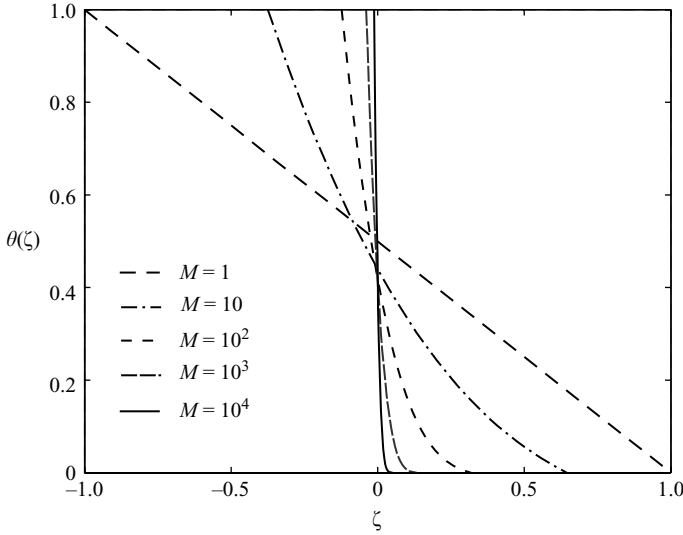


FIGURE 4. The similarity solution is shown for different values of  $M$ . The variable  $\theta$  is the non-dimensional thickness of the released fluid. It is measured from the top of the layer for a buoyant current.

that  $\Pi_1$  is finite. Following the procedure given by Barenblatt (1996), we assume complete similarity in the parameter  $\Pi_2$ , and we seek a solution of the form  $\Pi = \psi[\Pi_1, 0, \Pi_3] = \theta[\Pi_1, \Pi_2]$ . The expressions for  $\hat{h}$  and  $\hat{x}$  in these variables are

$$\hat{h} = H\theta[\zeta, M], \quad \hat{x} = \zeta[M](\kappa Ht)^{1/2}. \quad (3.3)$$

Dimensional analysis shows that the tip propagation is proportional to  $t^{1/2}$  when this scaling analysis is valid. The inner tip position is given by  $\hat{x}_i = \zeta_i[M](\kappa Ht)^{1/2}$ , and the outer tip position by  $\hat{x}_o = \zeta_o[M](\kappa Ht)^{1/2}$ , where  $\zeta_i$  and  $\zeta_o$  are dimensionless quantities that depend only on the mobility ratio  $M$ . Substituting relationships (3.3) into (2.2), we obtain a nonlinear ordinary differential equation for  $\theta$ :

$$-\frac{\zeta}{2} \frac{d\theta}{d\zeta} = \frac{d}{d\zeta} \left( \frac{\theta(1-\theta)}{\theta(M-1)+1} \frac{d\theta}{d\zeta} \right). \quad (3.4)$$

The mobility ratio  $M$  is the only parameter determining the shape of the similarity solution at early times. The inner and outer boundaries of integration,  $\zeta_i$  and  $\zeta_o$ , are unknown, and must be determined as part of the solution. The boundary conditions are:

$$\theta(\zeta_i) = 1, \quad \left. \frac{d\theta}{d\zeta} \right|_{\zeta_i} = \frac{\zeta_i M}{2}, \quad \theta(\zeta_o) = 0, \quad \left. \frac{d\theta}{d\zeta} \right|_{\zeta_o} = -\frac{\zeta_o}{2}.$$

The boundary conditions on  $\theta$  are the non-dimensional form of (3.1), and the conditions on  $d\theta/d\zeta$  come from inserting the conditions on  $\theta$  into (3.4). Equation (3.4) and the boundary conditions are invariant under reflection in  $\zeta$ , so that if  $\theta_1(\zeta)$  is a particular solution  $\theta_1(-\zeta)$  is also a solution. The physical interpretation of this reflection is exchanging the position of the fluids on either side of the initially vertical interface. The evolution of the interface at early times has been reduced to a nonlinear eigenvalue problem for a second-order ordinary differential equation, with two unknown eigenvalues and four boundary conditions. The two additional boundary conditions allow the unique determination of the eigenvalues as a function

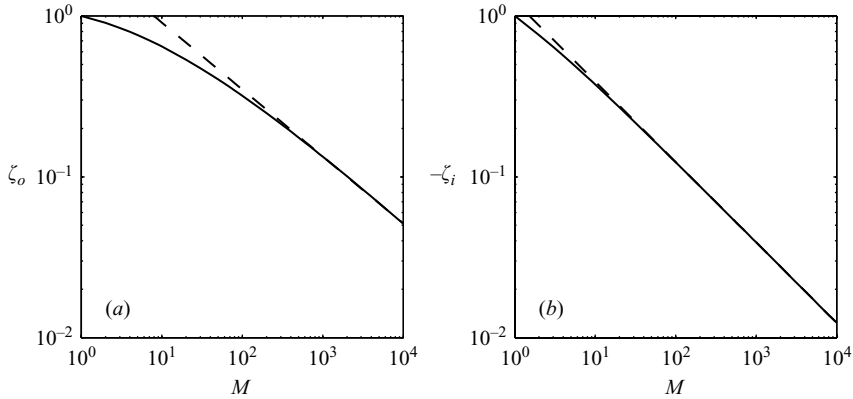


FIGURE 5. The numerical values for the outer (a) and inner (b) tip positions are shown as a function of  $M$  (solid lines). The scaling laws (3.6) and (3.7) are shown as dashed lines.

of the mobility ratio  $M$ . For unit mobility ratio (3.4) reduces to a simpler equation,

$$-\frac{\zeta}{2} \frac{d\theta}{d\zeta} = \frac{d}{d\zeta} \left( \theta(1-\theta) \frac{d\theta}{d\zeta} \right), \quad (3.5)$$

obtained by Huppert & Woods (1995). The solution is symmetric with respect to the origin, and the eigenvalues become  $\zeta_i = -\zeta_o = 1$ . Huppert & Woods (1995) have obtained the solution  $\theta = (1 + \zeta)/2$ . We note that  $\zeta_i = -\zeta_o = -1$  and  $\theta = (1 - \zeta)/2$  is also a solution. In the numerical solutions for the case  $M \neq 1$  we have chosen  $\zeta_i < 0$  and  $\zeta_o > 0$  (see figure 4). This choice places the released fluid on the left side and the ambient fluid on the right side of the tilting interface, and is consistent with geometry shown in figure 3.

### 3.2. Numerical solution of eigenvalue problem

The nonlinear eigenvalue problem has been solved numerically for the shape of the interface and the tip positions as a function of  $M$ . We only need to obtain numerical solutions for  $M > 1$ ; the corresponding solutions for  $M < 1$  can be obtained from the transformation (2.3). The eigenvalue problem has been solved using a shooting method, where we have integrated inward from both boundaries of the domain. The mismatch of  $\theta$  and  $d\theta/d\zeta$  at the origin was minimized to determine the eigenvalues for a given value of  $M$ . The analytic solution for  $M = 1$  was used as an initial guess for  $\zeta_i$  and  $\zeta_o$ , and  $M$  was increased incrementally to obtain solutions for  $M > 1$ . The resulting interface shapes are shown in figure 4.

As the mobility ratio increases a gravity tongue develops along one of the horizontal boundaries. In the limit of  $M \rightarrow \infty$  the interface appears to approach a vertical line. The viscosity of the released fluid  $\mu_p$  is kept constant, because the similarity variable  $\zeta$  depends on  $\mu_p$  through  $\kappa_p$ . Therefore, as we increase  $M = \mu_q/\mu_p$  we increase  $\mu_q$ , and in the limit  $\mu_q \rightarrow \infty$  the ambient fluid becomes immobile and the interface remains vertical.

Figure 5(a, b) shows the position of the inner and outer tip as a function of increasing mobility ratio. For large values of  $M$  the tip positions follow scaling laws given by

$$\zeta_i = -e^{0.2210} M^{-0.4997} \approx -\frac{1.24}{\sqrt{M}} \quad \text{for } M > 10, \quad (3.6)$$

$$\zeta_o = e^{0.8645} M^{-0.4163} \approx \frac{2.37}{M^{0.42}} \quad \text{for } M > 200, \quad (3.7)$$

which are shown as dashed lines in figure 5. The outward propagating non-dimensional tip position for  $M < 1$  is obtained from the following argument:

$$\hat{x}_o[M_p < 1] = -\hat{x}_i[M_q > 1] = -\zeta_i[M_q](\kappa_q Ht)^{1/2} = -\zeta_i[M_p^{-1}] \left( \frac{\kappa_p Ht}{M_p} \right)^{1/2}.$$

The inward propagating tip  $x_i[M_p < 1]$  can be obtained by an analogous argument. The self-similar tip positions for  $M < 1$  are given by  $\zeta_o[M < 1] = -\zeta_i[M^{-1}]/\sqrt{M}$  and  $\zeta_i[M < 1] = -\zeta_o[M^{-1}]/\sqrt{M}$ . The position of the outward propagating tip of the interface at early times is given by

$$x_o^e = \begin{cases} L_d + \zeta_o[M](\kappa Ht)^{1/2}, & M \geq 1, \\ L_d - \zeta_i[M^{-1}] \left( \frac{\kappa Ht}{M} \right)^{1/2}, & M < 1, \end{cases} \quad (3.8)$$

where the superscript  $e$  is used to indicate the scaling for the early similarity solution. The position of the inward propagation tip is given by

$$x_i = \begin{cases} L_d + \zeta_i[M](\kappa Ht)^{1/2}, & M \geq 1, \\ L_d - \zeta_o[M^{-1}] \left( \frac{\kappa Ht}{M} \right)^{1/2}, & M < 1. \end{cases} \quad (3.9)$$

The numerical values of  $\zeta_o$  and  $\zeta_i$  can be obtained from figure 5 or from (3.6) and (3.7) in the appropriate limits.

### 3.3. Range of validity of the early similarity solution

The similarity solutions described above were obtained under the assumption of complete similarity in  $\Pi_2$ , which corresponds to a step function initial profile ( $L_f = 0$ ). Barenblatt & Zeldovich (1972) have shown that similarity solutions are intermediate asymptotic solutions for a much larger class of initial conditions. Therefore, the analysis presented above also applies to initial profiles with a finite front width ( $L_f \neq 0$ ), for which  $\Pi_2 \neq 0$ . For this larger class of initial conditions the similarity solution will be valid after the details of the initial conditions have dissipated, because  $\Pi_2 = L_f/(\kappa Ht)^{1/2}$  approaches zero for  $L_f \ll (\kappa Ht)^{1/2}$ . Hence every particular initial condition will be asymptotic to the similarity solution for

$$t \gg t_e = \frac{L_f^2}{\kappa H}. \quad (3.10)$$

This is illustrated for a particular initial condition in figure 6(a). The initial condition is a ramp defined by

$$\hat{h}_0 = \begin{cases} 0, & \hat{x} < -0.5, \\ \hat{x} + 0.5, & -0.5 \leq \hat{x} \leq 0.5, \\ 1, & \hat{x} > 0.5. \end{cases} \quad (3.11)$$

In this case  $L_f = \kappa = H = 1$ , and we have chosen a mobility ratio of  $M = 10$ . The partial differential equation (2.2) was solved numerically (see § 5.1), and the solutions at various times are plotted as dashed lines. The similarity solution obtained from the eigenvalue problem is shown for comparison. The particular solution is essentially identical to the similarity solution at  $t = 10$ , which is only an order of magnitude larger than the lower bound  $t_e = 1$ .

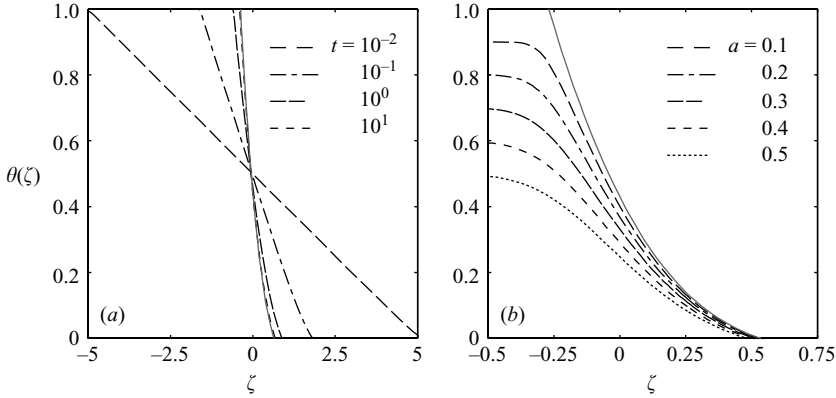


FIGURE 6. (a) The numerical solution to (2.2) with initial condition (3.11) and  $M=10$  is plotted at various times  $t$  and compared to the self-similar solution obtained from (3.4) (solid grey line). (b) Numerical solutions to (2.2) with  $M=20$  and initial condition (3.14) are shown for several values of the parameter  $a$  in the initial condition and compared to the solution of (3.4) with  $a=0$  (solid grey line).

For  $t \gg t_e$  the similarity solution is valid until the inward propagating tip reaches the origin  $x_i(t_b) = 0$ , where  $t_b$  is the back-propagation time (figure 1b). Solving (3.9) for  $t_b$  we obtain

$$t_b = \begin{cases} \frac{L_d^2}{\kappa H \zeta_i [M]^2}, & M \geq 1, \\ \frac{L_d^2 M}{\kappa H \zeta_o [M^{-1}]^2}, & M < 1. \end{cases} \tag{3.12}$$

Hence the early self-similar solution is valid for  $t_e \ll t \ll t_b$ . We can also define a new length scale  $L_b = 2x_o(t_b)$ , the width of the current at the back-propagation time. For small  $M$ ,  $L_b$  provides a suitable initial length scale for the late similarity solution in §4.  $L_b$  is given by

$$L_b = \begin{cases} 2L_d \left( 1 + \frac{\zeta_i [M^{-1}]}{\zeta_o [M^{-1}]} \sqrt{M} \right), & M < 1, \\ 2L_d \left( 1 + \frac{\zeta_o [M]}{\zeta_i [M]} \right), & M \geq 1. \end{cases} \tag{3.13}$$

In some situations the released fluid may not fill the entire depth of the domain. So that the idealized initial condition is given by

$$h_0^* = \begin{cases} H - a & \text{for } |x| \leq L_d, \\ 0 & \text{for } |x| > L_d, \end{cases} \tag{3.14}$$

where  $a < H$  is the thickness of the ambient fluid in the injection zone. Figure 6(b) compares numerical solutions to (2.2), with  $M=20$  and for various values of  $a$ , with the solution to (3.4), which corresponds to  $a=0$ . Solutions for  $a \neq 0$  are also self-similar in the early similarity variable, so that the outward propagating tip propagates as  $t^{1/2}$  for  $a \neq 0$ . The position of the tip  $\zeta_o$  in self-similar coordinates decreases with increasing  $a$ , but for  $a/H < 0.2$  the difference is less than 10% compared to the values of  $\zeta_o$  given in figure 5(a). The evolution of currents that do not fill the layer entirely

behave similar to those investigated here, and follow the same early scaling law. The viscosity of the ambient fluid cannot be neglected even if the released fluid does not fill the layer entirely. A full investigation of this larger family of similarity solutions for  $a \neq 0$  is beyond the scope of this investigation.

#### 4. Self-similar solution at late times

##### 4.1. Reduction to the porous medium equation

At the back-propagation time  $t_b$  the interface detaches from one of the horizontal boundaries, and the thickness of the released fluid  $h$  decreases monotonically as a function of time (figure 1c, d). At late times  $h \ll H$ , and we expect the solution for a finite layer to be similar to the solution in a half-space. The equation for the half-space can be obtained from (2.2) by taking the limit for  $H \rightarrow \infty$ , for finite  $h$  and  $M$ , or equivalently taking the limit  $h \rightarrow 0$ , for finite  $H$  and  $M$ . Consider the limit of the nonlinear diffusion coefficient in (2.2) for small  $h$ , keeping  $M$  and  $H$  constant:

$$\lim_{h \rightarrow 0} \frac{h(H-h)}{h(M-1)+H} = h. \quad (4.1)$$

In this limit (2.2) reduces to the porous medium equation

$$\frac{\partial h}{\partial x} = \kappa \frac{\partial}{\partial x} \left( h \frac{\partial h}{\partial x} \right), \quad (4.2)$$

which has been studied intensively, and the similarity solution for a finite release of fluid into a two-dimensional porous half-space was found by Barenblatt (1952).

We expect that the limit (4.1) becomes a good approximation even if  $h \ll H$  is finite, and (4.2) becomes a good approximation for (2.2) after some time. The parameter  $M$  can vary over several orders of magnitude, and we need to consider its effect on the validity of approximation (4.1). Consider the approximation in the denominator of (4.1) for finite but small values of  $h$ :

$$h(M-1)+H \approx H.$$

Large values of  $M$  require even smaller values of  $h$  to allow this approximation. Since  $h$  is a monotonically decreasing function of time, the half-space approximation will become valid for all  $M$  eventually. In §5.2 we develop an expression for the onset of half-space behaviour as a function of  $M$ . For small  $M$  the half-space approximation becomes valid very quickly. In the limit of small a mobility ratio we obtain

$$\lim_{M \rightarrow 0} \frac{h(H-h)}{h(M-1)+H} = h, \quad (4.3)$$

and (2.2) reduces to (4.2) at all times and for all values of  $h$  and  $H$ . As mentioned in §1.2, the simplification in this limit is responsible for the success of (4.2) in problems of unconfined flow, where the ambient fluid is a gas ( $M \ll 1$ ).

Equation (4.2) only depends on the mobility of the released fluid  $\lambda_p$ , not on the mobility ratio  $M$ . From the global conservation of mass  $Q_p + Q_q = 0$ , we can obtain an expression for the Darcy velocity  $q_q$  in the ambient fluid:

$$q_q = -\frac{h_p q_p}{(H-h_p)}. \quad (4.4)$$

For finite  $h_p$  and  $q_p$  the flux in the ambient fluid  $q_q$  becomes negligible as  $H \rightarrow \infty$ . In contrast to the early evolution, where  $M$  is the governing parameter, the problem

becomes independent of the mobility ratio at late times, because the ambient fluid is stationary.

4.2. *Barenblatt's solution*

In either limit the initial condition for the porous medium equation is a particular gas distribution  $\tilde{h}[x]$ , with finite width  $L_b$ , in a half-space otherwise saturated by water. The volume of current is given by

$$V = \int \tilde{h}[x]dx = 2L_dH. \tag{4.5}$$

A similarity solution in the parameters

$$h = \left(\frac{V^2}{\kappa t}\right)^{1/3} \varphi[\xi] \quad \text{and} \quad x = \xi(\kappa Vt)^{1/3} \tag{4.6}$$

has been found by Barenblatt (1952) and is given by

$$h[x, t] = \begin{cases} \frac{1}{6} \left(\frac{V^2}{\kappa t}\right)^{1/3} \left(\xi_o^2 - \frac{x^2}{(\kappa Vt)^{2/3}}\right) & \text{for } |x| \leq x_o^l, \\ 0 & \text{for } |x| > x_o^l. \end{cases} \tag{4.7}$$

From the definition of the self-similar coordinate  $\xi$ , the tip propagation at late times is proportional to  $t^{1/3}$ , and the front position at late time is given by

$$x_o^l = (9\kappa L_d Ht)^{1/3}. \tag{4.8}$$

The superscript  $l$  identifies the tip scaling for the late similarity solution. The late similarity solution depends on the volume of the released fluid  $V = 2L_dH$ , but it is independent of the local length scale  $L_f$  of the initial front, and the mobility ratio  $M$ . In contrast, the early tip scaling (3.8) is independent of the global length scale  $L_d$ , but depends on  $L_f$  and  $M$ .

The similarity solution obtained for the idealized initial condition is an intermediate asymptotic solution for a larger range of initial conditions with  $L_b \neq 0$ , for times larger than

$$t \gg t_l = \tilde{t} + \frac{L_b^3}{2\kappa_g L_d H}, \tag{4.9}$$

where  $\tilde{t}$  is the time at which (4.1) becomes valid. This lower bound becomes important when  $M \ll 1$ , and the porous medium equation becomes valid very quickly. In this case  $\tilde{t} = t_b$ , and (3.13) is a suitable initial length scale  $L_b$ , so that  $t_l$  becomes

$$t_l = \frac{L_d^2}{\kappa H} \left( 8 \left( \frac{1 + \sqrt{M}\zeta_i[M^{-1}]}{\zeta_o[M^{-1}]} \right)^3 - \frac{M}{\zeta_o[M^{-1}]^2} \right). \tag{4.10}$$

5. **Non-self-similar transition**

We have obtained a description of the front propagation speed at early times from the similarity solution describing a tilting interface (§3). At late times the governing equations simplify to (4.2), and the similarity solution of Barenblatt (1952) gives the propagation speed at late times. The transition from the early to the late similarity solution will not be self-similar, and must be investigated numerically.

For the numerical solution of (2.2) we have chosen the following non-dimensional variables:  $\eta = h/H$ ,  $\chi = x/L_d$ , and  $\tau = t/t^*$  with the characteristic time  $t^* = L_d^2\kappa^{-1}H^{-1}$ .

Substituting these definitions into (2.2), we obtain the following dimensionless equation:

$$\frac{\partial \eta}{\partial \tau} = \frac{\partial}{\partial \chi} \left( \frac{\eta(1-\eta)}{\eta(M-1)+1} \frac{\partial \eta}{\partial \chi} \right). \quad (5.1)$$

The dimensionless mobility ratio  $M$  is the only governing parameter. We consider initial distributions that are symmetric with respect to the origin, so that we only need to consider the spatial domain  $[0, a]$  where  $a > 0$  is chosen larger than the maximum propagation distance estimated from (4.8). The initial condition in all simulations is the following step function:

$$\eta[\chi, \tau = 0] = \begin{cases} 1, & \chi \leq 1, \\ 0, & \chi > 1. \end{cases} \quad (5.2)$$

The problem is symmetric with respect to the origin, so that the boundary condition at the origin is  $\partial \eta(0, \tau) / \partial \chi = 0$ , and the outer boundary condition is  $\eta(a, \tau) = 0$ .

### 5.1. Finite volume discretization

The spatial domain was divided into  $N$  grid cells of width  $\Delta \chi$  centred at  $\chi_i = (i - 1/2) \Delta \chi$ , where  $i \in [1, N]$ . The temporal domain has been divided into  $M$  constant time steps of size  $\Delta \tau$ , so that the solution is obtained at times  $\tau_n = n \Delta \tau$ , for  $n \in [1, M]$ . The numerical approximation of the cell average in the  $i$ th cell is given by

$$\int_{\chi_{i-1/2}}^{\chi_{i+1/2}} \eta(\chi, \tau_n) \, d\chi = \eta_i^n + \mathcal{O}(\Delta \chi^2).$$

The right-hand side of (5.1) was discretized in divergence form to ensure discrete conservation (Leveque 2002), and central differences were used for all spatial derivatives. The time derivative was discretized using the explicit forward Euler method with a constant time step  $\Delta \tau$ . The update formula is given by

$$\eta_i^{n+1} = \eta_i^n - \frac{\Delta \tau}{\Delta \chi} (F_{i+1/2}^n - F_{i-1/2}^n). \quad (5.3)$$

The numerical flux function  $F_{i+1/2}^n = \mathcal{F}[\eta_i^n, \eta_{i+1}^n]$  is given by

$$\mathcal{F}[\eta_i^n, \eta_{i+1}^n] = -\frac{\eta_{i+1/2}^n (1 - \eta_{i+1/2}^n)}{\eta_{i+1/2}^n (M-1) + 1} \frac{\eta_{i+1}^n - \eta_i^n}{\Delta \chi}, \quad (5.4)$$

where  $\eta_{i+1/2}^n = (\eta_{i+1}^n + \eta_i^n) / 2$ . The numerical results were validated against the early similarity solution derived in §3 (see figure 6a).

### 5.2. Transition time

The two examples in figures 7(a) and 7(b) show the numerical transition from the early to the late similarity solution. The initial condition is the early similarity solution at the non-dimensional back-propagation time  $\tau_b$  given by

$$\tau_b = \begin{cases} \frac{1}{\zeta_i [M]^2}, & M \geq 1, \\ \frac{M}{\zeta_o [M^{-1}]^2}, & M < 1. \end{cases} \quad (5.5)$$

In figure 7(a) the evolution is shown for  $M = 1/2$ . In this case the curvature of the early and the late similarity solution is of the same sign. The main difference between them is the slope at the origin, where the early similarity solution has a finite slope,

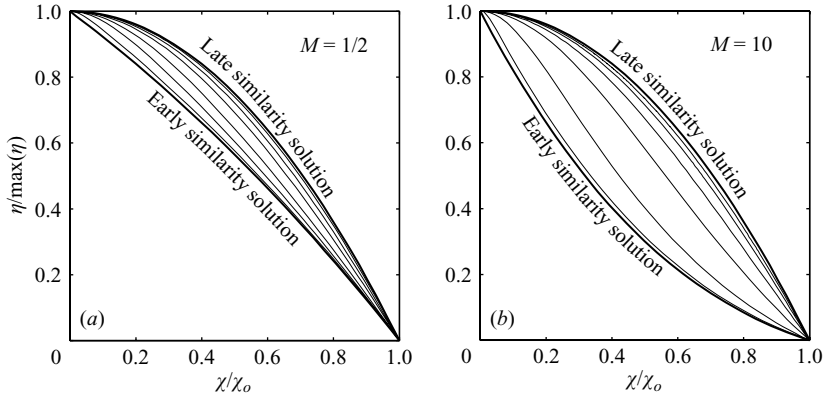


FIGURE 7. The transition of the numerical solution (light lines) from the early to the late similarity solution (both heavy lines) is shown in scaled coordinates. (a) The numerical solution is shown at  $\tau = \tau_b + \{1, 4, 10, 30, 100\}$ , where  $\tau_b = 0.61$ . (b) The numerical solution is shown at  $\tau = \tau_b + \{10^1, 10^2, 10^3, 10^4, 10^5\}$ , where  $\tau_b = 7.1$ .

but the late similarity solution has zero slope. In this case the transition period is relatively short, and the late similarity solution is a good approximation to the solution for  $\tau > 100$ . Figure 7(b) shows the transition for the case  $M = 10$ . In this case the curvature of the early and the late similarity solution is of opposite sign. The numerical solution adjusts very slowly and the transition period is very long.

### 5.3. Transition of the scaling for the tip position

Figure 8(a–d) shows the numerical results for the non-dimensional position of the outward propagating tip  $\chi_o$  of the released fluid as a function of non-dimensional time  $\tau$ . The figure shows the effect of increasing the mobility ratio  $M$  on the tip propagation and the timing of the transition. The scaling laws for the tip position obtained from the early and late similarity solutions are also shown. In non-dimensional coordinates these scaling laws (3.8, 4.8) simplify to

$$\chi_o^e = \begin{cases} 1 + \zeta_o [M] \tau^{1/2}, & M \geq 1, \\ 1 - \zeta_i [M^{-1}] \tau^{1/2} M^{-1/2}, & M < 1, \end{cases} \quad (5.6)$$

$$\chi_o^l = (9\tau)^{1/3}, \quad (5.7)$$

respectively. The shifted tip position  $\chi_o - 1$  is plotted as a function of time in logarithmic axes, so that the early scaling law (5.6) plots as a straight line with slope 1/2. In these variables the late scaling law (5.7) does not plot as a straight line, but it approaches a straight line with slope 1/3 for large times, where it becomes valid. The late scaling law is independent of  $M$  and therefore the same curve in all four figures, while the straight line corresponding to the early similarity solution is shifting downward as  $M$  increases. Comparison of the numerical results with the scaling laws from the early and late similarity solutions leads to the following four observations.

(a) The numerical tip position initially follows the early scaling law  $\chi_o \propto \tau^{1/2}$ , and then the scaling law for late times  $\chi_o \propto \tau^{1/3}$ .

(b) The transition time  $\tau_t$  increases monotonically with increasing  $M$ . Comparison of figures 8(a) and 8(b) shows that this increase is very small for  $M < 10^{-1}$ . Figures 8(c) and 8(d) show a rapid increase of the transition time for  $M > 10^{-1}$ .

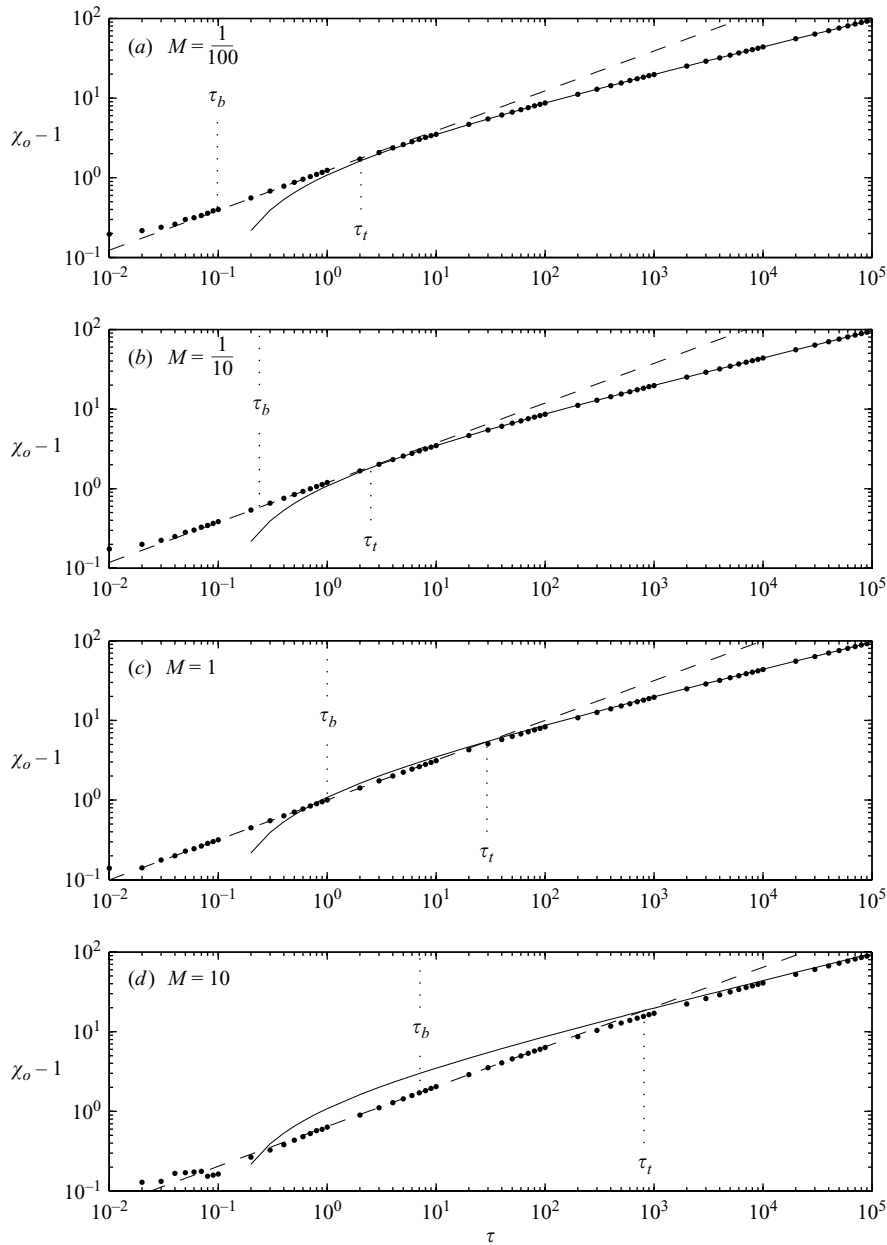


FIGURE 8. The numerical results for the non-dimensional tip position  $\chi_o$  are shown as a function of non-dimensional time  $\tau$ , for different mobility ratios  $M$ . In all figures the numerical solution is given by dots ( $\cdot\cdot\cdot$ ), the tip scaling from the early similarity solution by a dashed line ( $- - -$ ), and the tip scaling from the late similarity solution as a full line ( $—$ ). (a)  $\tau_t = 2.0$ ,  $\tau_b = 0.1$ ; (b)  $\tau_t = 2.5$ ,  $\tau_b = 0.24$ ; (c)  $\tau_t = 29.3$ ,  $\tau_b = 1$ ; (d)  $\tau_t = 811.3$ ,  $\tau_b = 7.1$ .

(c) The transition from the early to the late scaling is short for  $M \approx 10^{-1}$  (figure 8b), and increases rapidly for  $M > 10^{-1}$  (figure 8d).

(d) The tip position follows the early scaling law  $\chi_o \propto \tau^{1/2}$  even after the early similarity solution has become invalid at  $\tau_b$  (5.5). In figure 8(a–c) the early scaling

law continues to be valid almost up to  $\tau_t$ . This shows that the finite depth of the layer continues to have a strong effect on the solution, even after the interface has detached from one of the boundaries.

Although the early and the late scaling behaviour are separated by a transition period, it is useful to define a dimensionless transition time  $\tau_t$  that falls within this transition period. This transition time defines a lower bound for the validity of the late similarity solution. The difference between the early and the late scaling law is given by

$$f[\tau; M] = (\chi_o^l - 1) - \chi_o^e, \tag{5.8}$$

where  $\chi_o^l$  is given by (5.7), and  $\chi_o^e$  by (5.6). We use the substitution  $\tau = y^6$  to eliminate  $\tau^{1/2}$  and  $\tau^{1/3}$  and obtain a cubic in  $y$ . Let  $M_t$  denote the value of  $M$ , where the early scaling law is tangent to the late scaling law such that  $f(\tau; M_t) = 0$ . For  $M \geq M_t$  the non-dimensional transition time  $\tau_t$  can be defined as the intersection of the early and late time scaling laws (figure 8c, d), and is therefore given by the largest real root of  $f(\tau; M \geq 1) = 0$ . For  $M < M_t$  the two scaling laws do not intersect, but the transition time can be defined as the point of minimal vertical distance between the two scaling laws (figures 8c and 8d) given by the local minimum of (5.8). Solving for the appropriate root and the minimum, we obtain the following expression for the non-dimensional transition time,

$$\tau_t = \begin{cases} \frac{1}{9\zeta_o [M]^6} \left( 1 + 2 \cos \left[ \frac{\pi}{3} - \frac{\theta}{3} \right] \right)^6, & M \geq 1, \\ \frac{M^3}{9\zeta_i [M^{-1}]^6} \left( 1 + 2 \cos \left[ \frac{\pi}{3} - \frac{\theta}{3} \right] \right)^6, & M_t \leq M \leq 1, \\ \frac{64M^3}{9\zeta_i [M^{-1}]^6}, & M \leq M_t, \end{cases} \tag{5.9}$$

where  $\theta$  is the principle argument of the following complex numbers,

$$\theta = \begin{cases} \text{Arg}[-2 + 3\zeta_o[M]^2 + i\zeta_o[M]\sqrt{12 - 9\zeta_o[M]}], & M \geq 1, \\ \text{Arg}[-2M^{3/2} + 3\sqrt{M}\zeta_i[1/M]^2 - i\zeta_i[1/M]\sqrt{3M(4M - 3\zeta_i[1/M]^2)}], & M_t \leq M \leq 1. \end{cases}$$

Owing to the change in the definition of the transition time at  $M_t$  the graph is not smooth at this point (figure 9). For  $M < M_t$  the transition time increases very slowly with  $M$ , while it increases strongly for  $M \geq M_t$  (figure 9).  $M_t$  can be obtained by finding the value of  $M$  for which the local minimum of (5.8) is zero, that is,

$$M_t - \frac{3}{4}\zeta_i [M_t^{-1}]^2 = 0. \tag{5.10}$$

This equation must be solved numerically, because  $\zeta_i[M_t^{-1}]$  is not known analytically, and we obtain  $M_t = 0.1839$ . For large values of  $M$ ,  $\chi_o(\tau_t) \gg 1$  and (5.8) simplifies to  $f \approx \hat{f} = \chi_o^l - \chi_o^e$  and gives a scaling law for the transition time  $\tau_t = 0.45M^{5/2}$ . For small values of  $M$ , (3.9) can be used to simplify (5.9) to obtain a constant  $\tau_t = 1.96$ . Equation (5.9) is complicated to evaluate, and we therefore introduce a simple expression based on the two limits discussed above and a simple fit for intermediate values:

$$\tau_t \approx \begin{cases} 0.45M^{5/2}, & 10^2 < M, \\ 36.6M^{3/2}, & M_t \geq M \leq 10^2, \\ 2, & M < M_t. \end{cases} \tag{5.11}$$

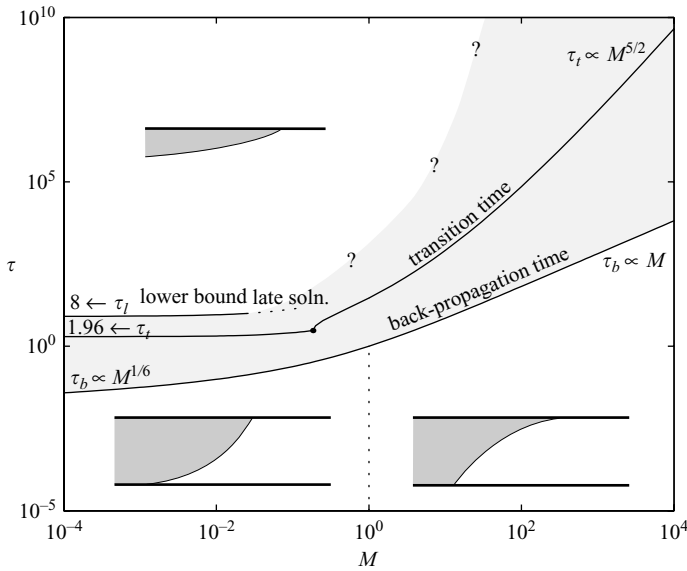


FIGURE 9. Regime diagram for a finite release of fluid into a horizontal porous slab, showing the non-dimensional time scales obtained in this study, and the shapes of the gravity current as a function of the mobility ratio  $M$ . The shaded region indicates the transition period between the similarity solutions. The characteristic time to dimensionalize all results is  $t^* = L_d^2 \kappa^{-1} H^{-1}$ .

### 6. Discussion

We have analysed the evolution of a finite release of fluid into a horizontal porous medium saturated with an ambient fluid. The released fluid can be miscible or immiscible with the ambient fluid. The density difference between the fluids is the only driving force that has been considered. We first summarize our results in a regime diagram. Then we illustrate the strong effect that the mobility ratio has on the tip propagation speed, by looking at the effect of switching released and ambient fluid on the laboratory experiments by Huppert & Woods (1995). Finally we discuss the implications of this study for CO<sub>2</sub> storage in saline aquifers, by considering some field examples.

#### 6.1. Regime diagram

Figure 9 combines all time scales into a  $M$ - $\tau$  regime diagram, that determines the evolution of a finite release of fluid. The only parameter in this problem is the mobility ratio  $M = M_p = \lambda_p / \lambda_q = \mu_q / \mu_p$  between the released fluid  $p$  and the ambient fluid  $q$ . The magnitude of a particular dimensional time scale is given by the characteristic time  $t^* = L_d^2 \kappa^{-1} H^{-1}$  formed from the displacement distance  $L_d$ , the diffusivity of the released fluid  $\kappa = \kappa_p$  and the height of the layer  $H$ . The mobility of the released fluid  $\lambda_p$  appears in  $\kappa_p$ , and  $\kappa_p$  enters the characteristic time  $t^*$  used for the non-dimensionalization; hence  $\lambda_p$  is constant and changes in  $M$  are due to changes in  $\lambda_q$ . For all finite values of  $M$  the evolution can be divided into three dynamic stages: an early self-similar regime, a transition period, and a late self-similar regime.

After the details of the initial condition have been lost, the interface is asymptotic to an early similarity solution that corresponds to a tilting interface. The early similarity variable is  $\zeta = x(\kappa H t)^{-1/2}$ , so that the non-dimensional tip position is given by  $\chi_o \propto \tau^{1/2}$ . During this period the left and the right interface evolve independently,

and the length scale of their separation  $2L_d$  does not appear in the similarity variable. In this phase both fluids move with non-zero velocity, and therefore the mobility ratio  $M$  determines the shape of the interface. We have not plotted the lower bound on the onset of the early similarity solution (3.10), because this time scale depends on the initial width of the front  $L_f$ ; in non-dimensional variables it is given by  $\tau_e = (L_f/L_d)^2$ . The early similarity solution ends at the back-propagation time  $\tau_b$ , because inward propagating tips of the two initially separated fronts start to interact at the origin (figure 1b). Figure 9 shows that  $\tau_b$  increases monotonically with time, and follows simple scaling laws for big and small  $M$ . Physically, we can explain the increase of  $\tau_b$  with increasing  $M$  by the increasing viscosity of the ambient fluid that slows down the inward propagating tip of the tilting interface. The period during which the early similarity solution is valid increases with increasing  $M$ , because the  $\tau_e \neq \tau_e[M]$ . As long as  $L_f \neq 0$  there are always values  $M \leq M_c$  such that  $\tau_e \geq \tau_b$ , and hence the early similarity solution is not realized.  $M_c$  is determined by the equation  $L_f/L_d = \sqrt{M_c/\zeta_o}[M_c^{-1}]$  for  $M_c < 1$ ; a similar equation can be found for  $M_c > 1$ . Even in the case  $L_f = 0$ , the early similarity solution will not be realized in the limit  $M \rightarrow 0$ , because  $\tau_b \rightarrow 0$ . Figure 8 shows that the scaling law for the non-dimensional tip position  $\chi_o \propto \tau^{1/2}$  is valid for a significant time after the early similarity solution itself has become invalid at  $\tau_b$ .

The initial similarity solution is followed by a period where the solution is not self-similar and must be obtained numerically (figure 7). For  $M \ll 1$  we can define the transition period as  $\tau_b < \tau < \tau_t$ , where  $\tau_t$  can be obtained from (4.10). The duration of the transition period increases as  $M \rightarrow 0$ , because the upper boundary is constant  $\tau_t = 8$ , while the lower boundary is proportional to  $\tau_b \propto M^{1/6}$ . For  $M > 1$  we have no estimate of the upper boundary of the transition period. The numerical results in figure 8(b–d) show that the transition period increases with increasing  $M$ . From the transition of the scaling laws for the tip position we have defined a transition time  $\tau_t$ , which provides a lower bound on the onset of the late similarity solution. Equation (5.9) or (5.11) shows a rapid increase of  $\tau_t$  with increasing  $M$  for  $M > M_t$ .

After the transition period the late similarity solution becomes valid, because the released fluid occupies only a small fraction of the height of the aquifer, and (2.2) reduces to (4.2). Equation (4.2) admits a similarity transformation in the variable  $\xi = x/(\kappa Vt)^{-1/3}$ , and the analytic solution has been obtained by Barenblatt (1952). In contrast to the early similarity solution, this late similarity solution is independent of the mobility ratio  $M$ , and depends on the volume of the current  $V = 2L_dH$ . In this limit the velocity of the ambient fluid is negligible, which explains why the problem is now independent of the mobility of the ambient fluid, and hence the mobility ratio  $M$ . When the late similarity solution is valid, the non-dimensional tip position is given by  $\chi_o \propto \tau^{1/3}$ . Again the scaling for the tip position becomes valid before the solution is fully self-similar.

## 6.2. The effect of switching released and ambient fluids

It is now clear that the mobility ratio has a strong effect on the evolution of the tip position (figure 9). Switching the released and ambient fluid in the finite release experiments reported by Huppert & Woods (1995) will illustrate this. They report the finite release of glycerin into an air-filled Hele–Shaw cell that serves as an analogue for a two-dimensional horizontal porous slab. The analogous permeability of the Hele–Shaw cell is  $k = 8.33 \times 10^{-6} \text{ m}^2$ , its height is  $H = 10 \text{ cm}$ , the initial width of the released fluid is  $L_d = 9 \text{ cm}$ , and the interface is vertical, so  $L_f = 0$ . The properties of the glycerin are  $\rho_g = 1260 \text{ kg m}^{-3}$  (personal communication by H. Huppert),  $\mu_g = 8.82 \times 10^{-1} \text{ Pa s}$ ,

the properties of air are  $\rho_a = 1.23 \text{ kg m}^{-3}$ ,  $\mu_a = 1.78 \times 10^{-5} \text{ Pa s}$ . The air properties are taken from Batchelor (1973). For a release of glycerin into an air-filled Hele–Shaw cell, the mobility ratio is very small,  $M_g \approx 2 \times 10^{-5}$ . The non-dimensional time scales are:  $\tau_b \approx 3 \times 10^{-2}$ ,  $\tau_t \approx 2$ , and  $\tau_l \approx 8$ . The dimensional time scales are obtained using the characteristic time  $t^* = L_d^2 \kappa_g^{-1} H^{-1} \approx 0.03 \text{ s}$ , so that  $t_b = \tau_b t^* \approx 10^{-3} \text{ s}$ ,  $t_t = \tau_t t^* \approx 0.06 \text{ s}$ , and  $t_l = \tau_l t^* \approx 0.24 \text{ s}$ , which is consistent with the observation by Huppert & Woods (1995) that the current had the shape of the late similarity solution 150 s after the release.

If, in contrast, the same volume of air is released into a glycerin-filled Hele–Shaw cell, the mobility ratio is very large,  $M_a \approx 5 \times 10^4$ . The non-dimensional time scales are:  $\tau_b \approx 3.2 \times 10^4$ , and  $\tau_t \approx 2.5 \times 10^{11}$ . The dimensional time scales are given by the characteristic time  $t^* = L_d^2 \kappa_a^{-1} H^{-1} \approx 7 \times 10^{-7} \text{ s}$ , so that  $t_b = \tau_b t^* \approx 0.02 \text{ s}$  and  $t_t = \tau_t t^* \approx 2 \text{ days}$ . Switching the ambient and the released fluid has increased the transition time between the early and the late similarity solution by many orders of magnitude. An experiment would have to be run for several days to reach the late similarity solution in this case. Huppert & Woods (1995) have reported that drag along the base causes the experimental current to lag behind the theoretical prediction. If the experiment must be run for such a long amount of time this may be a problem. On the other hand, the low viscosity of the air current may reduce this problem and allow experimental confirmation of our theoretical predictions. Lyle *et al.* (2005) perform experiments where viscous fluids are injected into a porous medium filled with air ( $M \ll 1$ ). They report good agreement with theoretical models based on the radial equivalent of (4.2), even when the height of the current is still a significant fraction of the height of the porous layer. This is not surprising, given our results that show that (2.2) reduces to (4.2) as  $M \rightarrow 0$ . The example calculation given above shows that these results cannot be applied to the problem of the release of a mobile phase into a less mobile phase. We are currently not aware of any experiments where  $M > 1$ .

### 6.3. $\text{CO}_2$ storage in saline aquifers

During  $\text{CO}_2$  storage in saline aquifers a highly mobile supercritical  $\text{CO}_2$ -rich vapour phase is released into a storage aquifer saturated by a less mobile aqueous brine. The mobility ratio is  $M > 1$ , and we expect an extended early period where the tip position is given by  $x \propto t^{1/2}$ . The theory developed above allows us to estimate the duration of this period  $t_b$ , and after which time we can expect the late scaling law to hold. Consider the example of the Sleipner injection site, on the Norwegian continental shelf (Metz *et al.* 2006). We assume an injection period  $t_0 = 40$  years. The physical properties of the Utsira formation used for  $\text{CO}_2$  storage at Sleipner are: height  $H \approx 200 \text{ m}$ , permeability  $k \approx 3 \times 10^{-12} \text{ m}^2$ , porosity  $\phi \approx 0.35$ . Picking intermediate values from the range of physical properties for fluids in a shallow cold aquifer, given by Nordbotten *et al.* (2005), we set  $\rho_c = 710 \text{ kg m}^{-3}$ ,  $\rho_b = 1100 \text{ kg m}^{-3}$ ,  $\mu_c = 0.05 \times 10^{-3} \text{ Pa s}$ , and  $\mu_b = 1 \times 10^{-3} \text{ Pa s}$ , so that  $M_c = 20$ . For this case the dimensionless time scales are given by  $\tau_b \approx 14$  and  $\tau_t \approx 2810$ . The characteristic time is  $t^* = L_d^2 \kappa_c^{-1} H^{-1}$ , and we see that both time scales will increase quadratically with the injection distance  $L_d$ , while they decrease with both increasing  $H$  and  $\kappa_c = kg \Delta \rho \mu_c^{-1} \phi^{-1} = 6.6 \times 10^{-4} \text{ m s}^{-1}$ . Consider the effect of increasing  $L_d$  from 1000 to 2000 m: the back-propagation time  $t_b = t_0 + \tau_b t^*$  increases from 43.4 to 53.5 years, and the transition time  $t_t = t_0 + \tau_t t^*$  increases from 720 to 2740 years. It is commonly assumed that  $\text{CO}_2$  needs to be stored for several thousand years. If this change in the propagation regime is not anticipated the extent of the plume will be severely overestimated after a few hundred years.

#### 6.4. Further research

The theory presented above is two-dimensional and therefore an application to three-dimensional field cases is limited. We are pursuing a similar analysis for a radially symmetric case. Such an analysis will allow simple estimates of the area affected by the CO<sub>2</sub>-plume. The most important physical process that has been neglected is the trapping of CO<sub>2</sub> as residual saturation in the wake of the migrating plume (Spiteri *et al.* 2005; Ozah *et al.* 2005). Residual saturation refers to immobile disconnected bubbles of CO<sub>2</sub>-vapour formed by capillary snap-off. This trapping mechanism reduces the volume of the CO<sub>2</sub>-plume over time. The same effect is also important in the migration of non-aqueous phase contaminants in hydrology (Hunt, Sitar & Udell 1995a; Bear & Ryzhik 1998). We plan to extend the discussion presented here to a simple model of residual trapping.

### 7. Conclusion

We have derived the equation governing the flow of two fluids in two-dimensional, horizontal porous layer. The evolution of a finite release of fluid is divided into three regimes. The mobility ratio  $M$  is the parameter that determines the magnitude of the non-dimensional time scales separating these regimes.

We have obtained new similarity solutions in the variable  $\zeta = x(\kappa H t)^{-1/2}$  that are valid at early times when the interface is tilting due to a horizontal exchange flow. These similarity solutions are a strong function of the mobility ratio  $M$ . In this regime the position of the tip of the interface is given by  $x \propto t^{1/2}$ . The numerical solution follows the early scaling law, for a long time after the interface has detached from one boundary. This indicates that the finite thickness of the aquifer remains important for  $M > 1$  and solutions assuming infinite depth are not valid until the current has become very thin.

In the limits  $h \rightarrow 0$  and  $M \rightarrow 0$  the governing equation simplifies to the porous medium equation. This equation admits a similarity solution in the variable  $\xi = x/(\kappa V t)^{-1/3}$ , where the position of the tip of the interface is given by  $x \propto t^{1/3}$ . We have obtained an expression for the transition time  $t_t$  from the  $t^{1/2}$  to the  $t^{1/3}$  scaling. The transition time  $t_t$  increases monotonically with  $M$ , but it is a weak function of  $M$  for  $M < 0.18$ , and increases rapidly for  $M > 0.18$ . The two self-similar regimes are separated by a transition period that is roughly centred on  $t_t$ . Numerical solutions to the governing partial differential equation are used to obtain solutions during the non-self-similar transition period. Numerical results show good agreement with the early and the late similarity solutions.

During CO<sub>2</sub> storage in saline aquifers  $M \approx 20$ , and the transition from the early to the late scaling is likely to occur within the first thousand years. It is therefore important to anticipate this change in the propagation regime when estimating the extent of the CO<sub>2</sub>-plume.

The authors would like to acknowledge helpful discussions with J. Nordbotten and H. Huppert. This research was supported by the Global Climate and Energy Project and the SUPRI-B reservoir simulation affiliates program, at Stanford University.

#### REFERENCES

- BACHU, S. 2003 Screening and ranking of sedimentary basins for sequestration of CO<sub>2</sub> in geological media in response to climate change. *Environmental Geology* **44**, 277–289.

- BARENBLATT, G. I. 1952 On some unsteady motions of fluids and gases in a porous medium. *Appl. Math. and Mech. (PMM)* **16**, 67–78.
- BARENBLATT, G. I. 1996 *Scaling, Self-Similarity, and Intermediate Asymptotics*. Cambridge University Press.
- BARENBLATT, G. I. & VISHIK, M. I. 1956 On the finite speed of propagation in the problems of unsteady filtration of fluid and gas in a porous medium. *Appl. Math. Mech. (PMM)* **20**, 411–417.
- BARENBLATT, G. I. & ZELDOVICH, YA. B. 1972 Self-similar solutions as intermediate asymptotics. *Ann. Rev. Fluid Mech.* **4**, 285–312.
- BATCHELOR, G. K. 1973 *An Introduction to Fluid Mechanics*. Cambridge University Press.
- BEAR, J. 1972 *Dynamics of Fluids in Porous Media*. American Elsevier.
- BEAR, J. & RYZHIK, V. 1998 On displacement of NAPL lenses and plumes in a phreatic aquifer. *Transp. Porous Media* **33**, 227–255.
- DIETZ, D. N. 1953 A theoretical approach to the problem of encroaching and by-passing edge water. *Akad. van Wetenschappen, Proc.* **V. 56 B**, 83–92.
- HUNT, J. R., SITAR, N. & UDELL, K. S. 1995 Nonaqueous phase liquid transport and cleanup. Part 1. Analysis of mechanisms. *Water Resour. Res.* **24**, 1247–1258.
- HUPPERT, H. E. 1982 Propagation of two-dimensional viscous gravity currents over a rigid horizontal surface. *J. Fluid Mech.* **121**, 43–58.
- HUPPERT, H. E. & WOODS, A. W. 1995 Gravity-driven flows in porous media. *J. Fluid Mech.* **292**, 55–69.
- LAKE, L. L. 1989 *Enhanced Oil Recovery*. Prentice-Hall.
- LEVEQUE, R. J. 2002 *Finite Volume Methods for Hyperbolic Problems*. Cambridge University Press.
- LYLE, S., HUPPERT, H. E., HALLWORTH, M., BICKLE, M. & CHADWICK, A. 2005 Axisymmetric gravity currents in a porous medium. *J. Fluid Mech.* **543**, 293–302.
- METZ, B., DAVIDSON, O., DE CONINCK, H., LOOS, M. & MEYER, L. (Eds.) 2006 *Special Report on Carbon Dioxide Capture and Storage*. Cambridge University Press.
- NORDBOTTEN, J. M., CELIA, M. A. & BACHU, S. 2005 Injection and storage of CO<sub>2</sub> in deep saline aquifers: Analytical solution for the CO<sub>2</sub> plume evolution during plume injection. *Transp. Porous Media* **58**, 339–360.
- OZAH, R. C., LAKSHMINARASIMHAN, S., POPE, G. A., SEPEHRNOORI, K. & BRYANT, S. L. 2005 Numerical simulation of the storage of pure CO<sub>2</sub> and CO<sub>2</sub>-H<sub>2</sub>S gas mixtures in deep saline aquifers. In *SPE Annual Technical Conference and Exhibition* (Dallas, TX).
- RIAZ, A. & TCHELEPI, H. A. 2006 Numerical simulation of immiscible two-phase flow in porous media. *Phys. Fluids* **18** 014104.
- SPITERI, E. J., JUANES, R., BLUNT, M. J. & ORR JR, F. M. 2005 Relative permeability hysteresis: Trapping models and application to geological CO<sub>2</sub> sequestration. In *SPE Annual Technical Conference and Exhibition* (Dallas, TX).
- TCHELEPI, H. A. 1994 Viscous fingering, gravity segregation and permeability heterogeneity in two-dimensional and three-dimensional flows. PhD thesis, Stanford University.
- YORTSOS, Y. C. 1995 A theoretical analysis of vertical flow equilibrium. *Transp. Porous Media* **18**, 107–129.